Anatomy of air entrapment in drop impact on a solid surface

Zhenlong Wu[1,*], Yihua Cao[2], Yufeng Yao[3]

[1] College of Energy and Power Engineering, Nanjing University of Aeronautics and Astronautics, Nanjing, 210016, China

[2] School of Aeronautic Science and Engineering, Beihang University, Beijing, 100191, China

[3] Department of Engineering Design and Mathematics, University of the West of England, Bristol, BS16 1GQ, U.K.

[*] Correspondence: jackilongwu@gmail.com

Abstract: When a drop impacts on a solid surface, a thin air film is entrapped first and later evolves into a spherical air bubble at the center inside the drop. The problem involves several complex physical processes, including two-phase fluid flow interactions, moving and deforming interfaces in space and time. In this paper, we dissect the whole air entrapment and evolution process from drop release at a certain height above the substrate to finally a spherical air bubble formation by direct numerical simulation. A detailed quantitative analysis of the various dynamic phenomena occurring at different stages is performed. The complex physical phenomena revealed by current high-fidelity numerical simulations are validated qualitatively against theoretical estimations and previous experimental observations, followed by quantitative comparisons with the theories and available experiments for the dimple, kink and air film. Finally, a new cognition of vortex ring evolution is proposed to explore further insights into the underlying physical mechanisms associated with the evolution of the entrapped air film in liquid-solid impact.

Keywords: Drops and bubbles

1. INTRODUCTION

The impacts of liquid droplets onto solid surfaces are omnipresent in both the natural world and various industrial applications, for example, raindrops falling onto a windscreen, spray coatings, inkjet printing, rainfall and icing on aircraft surfaces (Josserand and Thoroddsen, 2016; Wu, 2018; Yarin, 2006). In some of such applications, one of the main focuses is how to suppress air bubbles inside the droplets, as the appearance of air bubble can cause large detrimental effects, e.g., decreasing the uniformity of spray coatings and the precision of splash control in inkjet-based manufacturing. Although the phenomenon of air entrapment during drop impact on a solid surface has already been observed in experiments several decades ago (Chandra and Avedisian, 1991; Esmailizadeh and Mesler, 1986; Pumphrey and Elmore, 1990; Sigler and Mesler, 1990), the important role that the entrapped air would play has still not fully been understood ever since the very early investigation on drop impact dynamics over a century ago (Worthington, 1877).

Morphological evolution of the entrapped air is one of the most important considerations in the field. Thoroddsen et al. (2005) first described the overall evolution of the air disc with pinch-off of a droplet inside the bubble. Subsequently, Lee et al. (2012) verified the evolution by X-ray experiments. In summary, a full evolution process of air entrapment in drop impact on a solid surface can be divided into four phases, i.e., touchdown of the liquid drop, retraction and contraction of the entrapped air, pinch-off of the daughter droplet, and finally formation

of a spherical air bubble, as schematically depicted in FIGURE 1(a). The geometric characteristic parameters that will be employed later in this paper are illustrated in FIGURE 1(b).

Initially, the drop falls freely from a certain height above the solid surface. Immediately before the drop contacts the substrate, the shape of the bottom of the drop deforms due to the combined effects of the inertial pressure force of the drop and the lubrication pressure force of the underlying air being pushed out radially, forming a dimple on the liquid-gas interface and a kink at the outer edge. This kink expands radially and touches down, entrapping a thin air film in the gap between the drop and the substrate (Bouwhuis et al., 2012; Korobkin et al., 2008; Li and Thoroddsen, 2015; Mandre et al., 2009; Mani et al., 2010). This phase is called "touchdown" in this paper.

Subsequently, the entrapped air film is pulled by the surface tension and retracts rapidly towards the center of the air film, termed as "retraction". The retraction speed is governed by the balance between the surface tension and inertia, thus is often named as "inertial retraction" (Lee et al., 2012; Thoroddsen et al., 2005).

Following retraction, the air volume contracts in order to minimize the surface energy whilst the capillary waves are propagating towards the center, which is called "contraction". The contraction process is dominated by the capillary waves generated during the retraction phase (Lee et al., 2012). The capillary waves move much faster than the retracting air film with their amplitudes growing. On the other hand, the top of the air film reverses by the compressed air after the crest arrives at the center. When the crest touches the solid, a three-dimensional toroidal air bubble is formed (Thoroddsen et al., 2005). This toroid further contracts until its top is coalesced like a hat, pinching off a small daughter droplet inside the bubble at the center. Subsequently, the daughter droplet is gradually squeezed out by the pressure in the bubble, resulting in a bubble attached to or detached from the solid, depending on the contact angle (Lee et al., 2012).
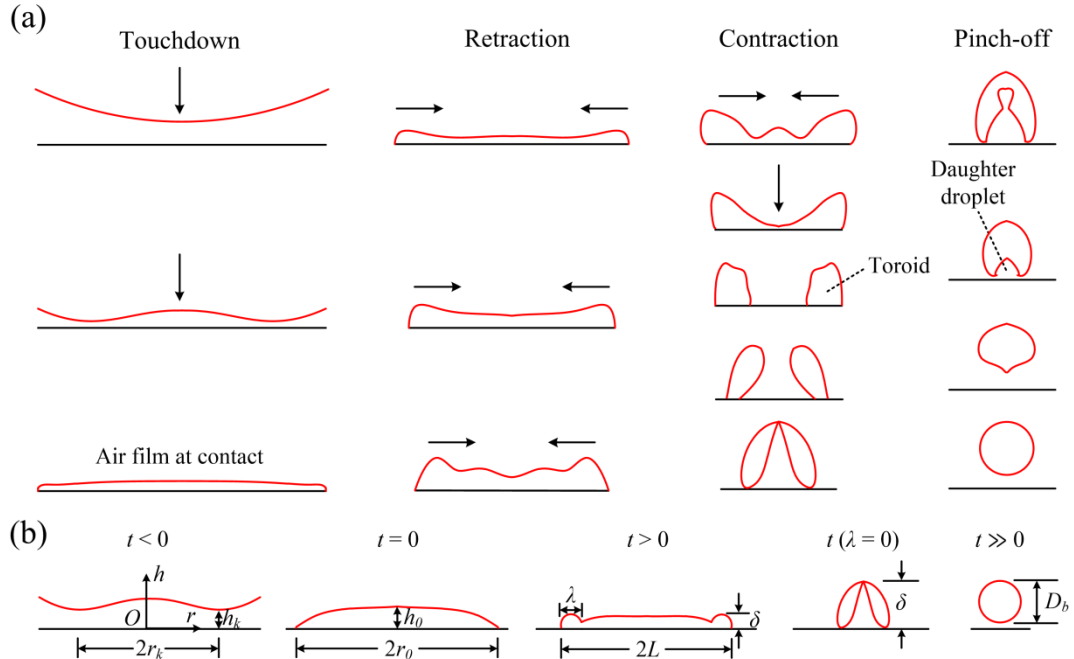

FIGURE 1. (a) Schematic views of the whole evolution process of the air entrapment during a liquid drop impact on a dry, solid surface: touchdown of the drop to form an air film, inertial retraction of the air film, viscous contraction of the rim to form a toroid, pinch-off of a daughter droplet to form a bubble attached to (not shown here) or detached from the solid surface. (b) Definition of the characteristic parameters of the air bubble profile after drop-surface contact. r and h are the general radial and axial coordinates, respectively, with the origin located at the center of the air film. The subscripts "k" and "0" denote the

variables related to the kink and the initial air film, respectively. L, λ and δ are the radius of the air film, the length and height of the rim, respectively. D_b is the diameter of the final spherical air bubble. The red curves stand for the interface between the air and the liquid drop, as well as the black lines for the solid surface and the black arrows for the drop falling and capillary wave propagation directions, respectively.

In retrospect, there are far less existing researches in the public domain on the air movement than for the liquid drop (Gargi et al., 2019; Oishi et al., 2019; Schroll et al., 2010; Xu et al., 2005). Due to the very small length scale of the entrapped air film (e.g., its height is typically of an order of $O(1)$ μm and the radius of an order of $O(100)$ μm, respectively), the majority of those published results related to air entrapment came either from drop impact experiments or theoretical analyses. Mehdi-Nejad et al. (2003) preliminarily characterized the air entrapment by solving the Navier-Stokes equations with a volume-of-fluid (VOF) method. Unfortunately, due to the limited computational resources at that time, the simulated morphology was not quite consistent with experimental observations.

Li et al. (2017) experimentally investigated the effects of reduced pressure on the air entrapment during a drop impact on a solid surface and observed a first entrapment of a central air film followed by a second outer entrapment of a circular band of air within the rarefied gas regime. Recently, Jian et al. (2020a) studied the air film contraction for drop impact on a liquid surface and observed three modes of the air contraction based on the local Ohnesorge number of the air film, i.e., a single bubble, a toroidal bubble in a similar way to that occurring in liquid-solid impacts and vertical splitting.
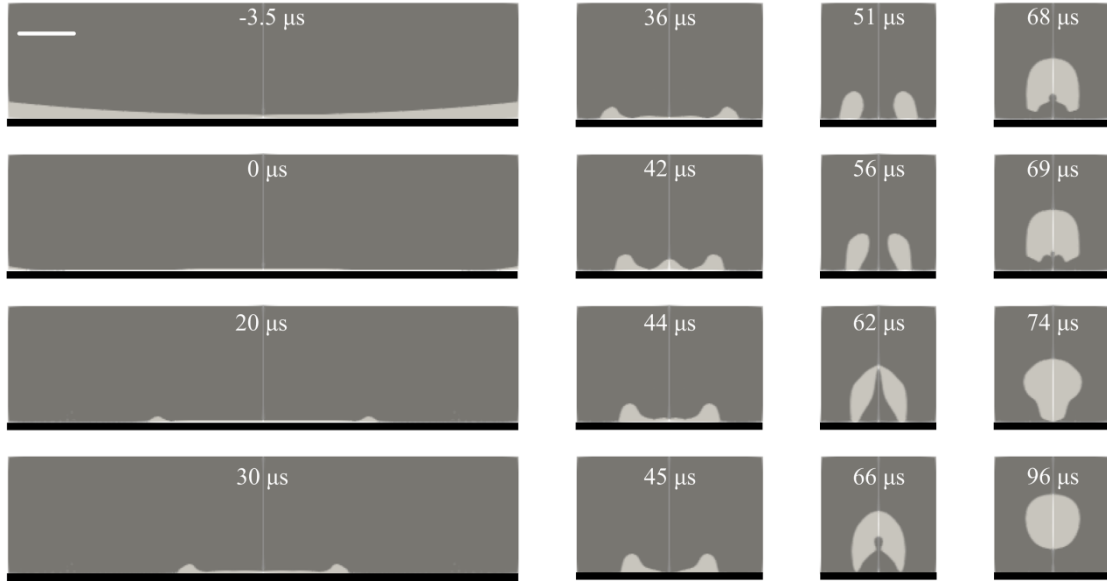

FIGURE 2. Evolution of an air film during the impact of a liquid (water) drop with a radius of 2 mm upon a dry, smooth, solid surface at an impact speed of V_0 = 2.97 m/s. Note that the instant when the drop first contacts the substrate is defined as the impact moment with the time set to be $t = 0$ μs in the whole paper. The dark grey, light grey and black colors represent the drop, air and substrate, respectively. The length of the scale bar shown in the first subgraph is 50 μm.

One of the biggest challenges faced by the implementation of computational fluid dynamics simulation of air entrapment lies in the large difference of the scales between the drop and the thin air film (Thoroddsen et al., 2005), which makes the motivations of the present study. In this paper, the whole evolution process of the air entrapment during a water drop impact on a dry smooth solid surface is investigated by direct numerical simulation.

The full compressible Navier-Stokes equations are considered for solving each fluid motion, together with a VOF method to capture the interface between the two phases using the "compressibleInterFoam" solver in the open source package OpenFOAM[®]. As the air entrapment occurs at the very beginning of the impact, i.e. in the early kinematic phase (Rioboo et al., 2002), the dynamics is assumed to be of the axisymmetric pattern, which has been validated rational in other similar studies in the field (Hicks et al., 2012; Jian et al., 2018; Mehdi-Nejad et al., 2003). The primary goal of this study is to conduct a much more detailed characterization of the whole entrapment and evolution process of the air film over a wide range of impact speeds. As an example, the whole air evolution at an impact speed of 2.97 *m/s* is shown in FIGURE 2. The characteristics of all the four phases are well captured and generally agree with the descriptions in FIGURE 1(a). The drop is released from a certain height above the substrate and later contacted with the substrate at $t = 0$ μs, entrapping a thin air film. Subsequently, the air film retracts inwards until the capillary wave arrives at the center at $t = 42$ μs and continues to contract until the top of the toroidal bubble coalesces at $t = 62$ μs. Following this, the toroidal bubble is gradually pinched off and eventually turns into a spherical bubble at $t = 96$ μs. All the four characteristic phases observed experimentally by Lee et al. (2012) have successfully been modeled in the present study. More quantitative results and details will be presented and analyzed in the later sections.

2. NUMERICAL IMPLEMENTATION

2.1. *Physical model*

We consider a spherical water drop with a radius $R = 2$ *mm*, density $\rho_l = 1000$ *kg/m³* and dynamic viscosity $\mu_l = 0.001 Pa \cdot s$ falling from a certain height above a solid surface and impacting normally to it at a velocity V_0, as shown in FIGURE 3(a). The drop dynamics can be described in the cylindrical coordinates r and z, where the z-axis is defined by the axis of symmetry of the problem, with the substrate located at $z = 0$, and r is the radial coordinate. The surrounding gas is air with density $\rho_g = 1.2$ *kg/m³*, dynamic viscosity $\mu_g = 1.776 \times 10^{-5}$ *Pa·s* and ambient pressure $p_0 = 1$ *atm*. The impact conditions are kept identical to the experimental conditions of Liu et al. (2013). The gravity effects have been carefully evaluated by running precursor cases with gravity excluded and it was found that there is no significant change in the morphology of the air bubble during the whole evolution process except for a very small time difference (e.g. less than 1 μs for the $V_0 = 2.97$ *m/s* case) at the end of the contraction phase, compared to the corresponding gravity-included case. Therefore, the gravity effects are not included in this study.

Two dimensionless parameters are usually used to characterize drop impact dynamics: Reynolds number Re and Weber number We, which are respectively expressed as,

$$Re = \frac{\rho_l V_0 R}{\mu_l} \tag{1}$$

$$We = \frac{\rho_l V_0^2 R}{\sigma} \tag{2}$$

The lubrication of gas layer is controlled by the Stokes number St defined as,

$$St = \frac{\mu_g}{\rho_l V_0 R} \tag{3}$$

In this study, all material properties have been kept as constant, except for the varying drop impact velocity $V_0 = 1.49 - 4.5$ _m/s_, corresponding to the Reynolds number $Re = 2980 - 9000$ and the Weber number $We = 88.8 - 810$, respectively.
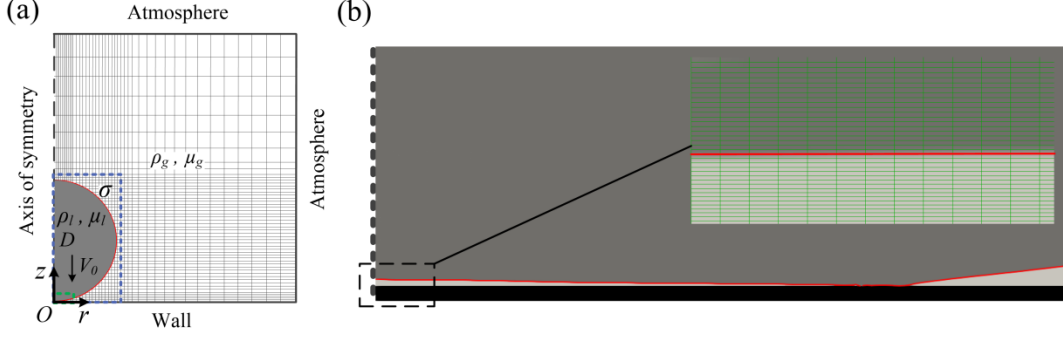

FIGURE 3. (a) Illustration of the impact model and the block-structured mesh topology adopted in this study. A two-dimensional axisymmetric simulation strategy is adopted. An inner block highlighted by a rectangle enclosed with the blue dashed lines sufficiently encases the region where the drop is present and filled with the finest grids in the air entrapment zone. The rest of the domain is filled with non-uniform grids. The red curve represents the drop-air interface. (b) A thin air film upon contact is well captured with the current meshing strategy. A magnified view of the grid in the central air entrapment region is shown in the inserted sub-figure.

2.2. _Mathematical model_

Interface or free surface tracking of two or more fluids has been a challenging task in multiphase flow modelling and simulation. Various methods have been developed so far, such as the Particles on Interface method (Daly, 1969), Height Function method (Nichols and Hirt, 1973), Level Set (LS) method (Osher and Sethian, 1988), Particles on Fluid method (Harlow and Welch, 1965) and Volume of Fluid (VOF) method (Hirt and Nichols, 1981). Compared with other methods, the VOF method is more computationally efficient because only the value of the volume fraction needs to be stored rather than the marker coordinates. So far, the VOF method has been widely used for drop impact simulations, such as air entrapment (Yeganehdoust et al., 2020), liquid sheet (Schroll et al., 2010), droplet splashing (Jian et al., 2018), thus it is employed here to track the interface between the air and water phases based on an Eulerian mesh. The compressible governing equations for each phase are written as follows (Nguyen et al., 2020):

$$\frac{\partial \rho}{\partial t} + \nabla \cdot (\rho \boldsymbol{u}) = 0 \tag{4}$$

$$\frac{\partial (\rho \boldsymbol{u})}{\partial t} + \nabla \cdot (\rho \boldsymbol{u} \boldsymbol{u}) = -\nabla p + \nabla \cdot \mathbf{T} + \boldsymbol{F}_\sigma \tag{5}$$

where ρ, μ, $\boldsymbol{u}$, t, and p denote the density, dynamic viscosity, velocity vector, time, and pressure, respectively. $\mathbf{T} = 2\mu \mathbf{S} - 2\mu (\nabla \cdot \boldsymbol{u}) \mathbf{I} / 3$ is the deviatoric viscous stress tensor where $\mathbf{S} = 0.5 \left[\nabla \boldsymbol{u} + (\nabla \boldsymbol{u})^T \right]$ is the mean rate of strain tensor. $\mathbf{I} = \delta_{ij}$ is Kronecker delta function. $\boldsymbol{F}_\sigma$ is the surface tension force.

The interface represented by an indicator function, i.e. volume fraction α $(0 \leq \alpha \leq 1)$, can be captured by solving the scalar transport equation for α as:

$$\frac{\partial \alpha}{\partial t} + \nabla \cdot (\boldsymbol{u}\alpha) = 0 \tag{6}$$

A cell with $\alpha=1$ means that it is fully occupied by water and that with $\alpha=0$ means it is fully occupied by air. Cells with volume fractions between unity and zero are considered to specify the interface between the two phases. Based on the cell volume fraction values, an interface is reconstructed by the Simple Line Interface Calculation (SLIC) technique (Noh and Woodward, 1976), which approximates the interface in each cell as a line parallel to one of the coordinate axes according to the value of the volume fraction. Taking a two-dimensional case as example, it results in two different situations: *x*-sweep and *y*-sweep, as shown in FIGURE 4 (b) and 4(c). To implement the SLIC method in multi-dimensions, it is necessary to use multiple one-dimensional sweeps to update the volume fraction at each time step. Concretely, the sequence of the sweeps normally alternates, e.g., if the *x*-sweep is done followed by the *y*-sweep at the present time step, then for the next step the sweep operation is done in the reverse order. It is worth noting that a new family of interpolation schemes based on the modern piecewise-linear interface calculation (PLIC) scheme (Youngs, 1984) is introduced in the latest version of OpenFOAM. This method represents the interface by surface-cuts splitting each cell to match the volume fraction of the phase in that cell, as shown in FIGURE 4(d). A comparison between the results obtained by both interface calculation schemes will be presented in the following subsection. For post-processing, the interface is described by the surface at $\alpha=0.5$.

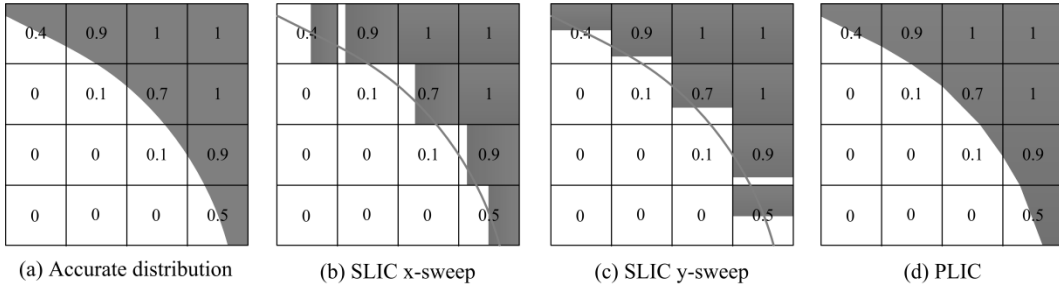(a) Accurate distribution   (b) SLIC x-sweep   (c) SLIC y-sweep   (d) PLIC

FIGURE 4. Illustration of the SLIC and PLIC interface reconstruction methods. The dark and white regions represent the liquid and gas phases, respectively. The number in each cell represents the value of volume fraction of liquid in each cell.

The VOF method assumes that the contributions of the liquid and gas variables to the evolution of the interface are proportional to the corresponding volume fraction of the respective fluid phase. The density ρ and viscosity μ across the interface are respectively replaced by

$$\rho = \rho_l \alpha + \rho_g (1-\alpha) \tag{7}$$

$$\mu = \mu_l \alpha + \mu_g (1-\alpha) \tag{8}$$

For interface-capturing methods, the interface is not tracked explicitly and thus its exact shape and location are unknown before simulation. There are two types of surface tension discretization methods that can be combined with VOF methods, i.e., the continuum surface force (CSF) method and the ghost fluid method (GFM) (Popinet, 2018). In the CSF model, the exact value of the phase volume fraction α is used and thus is closely related to the interface thickness, whereas the Heaviside function used in GFM takes the value of 1 only when $\alpha > 0.5$ and equals zero for other cases (Popinet, 2018). In this study the CSF method is employed to model the

surface tension force, which can be written as (Brackbill et al., 1992):

$$F_\sigma = \sigma\kappa\frac{\rho}{0.5(\rho_l + \rho_g)}\nabla\alpha \approx \sigma\kappa\nabla\alpha \tag{9}$$

where κ is the surface curvature formulated by local gradients along the normal direction (Hemida, 2008):

$$\kappa = \nabla\cdot\hat{\boldsymbol{n}} = \nabla\cdot\frac{\boldsymbol{n}}{|\boldsymbol{n}|} = \nabla\cdot\left(\frac{\nabla\alpha}{|\nabla\alpha|}\right) \tag{10}$$

The challenging aspect of the volume fraction transport equation (6) is to capture a sharp interface while maintaining both the boundedness and mass conservation in each single phase, as any small errors in the volume fraction across the interface can lead to considerable errors in the calculation of the physical properties. In the present study, the multi-dimensional universal limiter for explicit solution (MULES) scheme (Weller, 2008) is adopted, where an additional counter-gradient convective term originating from modeling the velocity in terms of weighted average of the corresponding liquid and gas velocities is introduced into the phase volume fraction transport equation to compress the interface thickness. Within the MULES scheme, the phase volume fraction transport equation (6) can be rewritten as

$$\partial_t\alpha + \nabla\cdot(\alpha\boldsymbol{u}) + \nabla\cdot[\boldsymbol{u}_c\alpha(1-\alpha)] = 0 \tag{11}$$

where $\boldsymbol{u}_c$ is called compression velocity (Berberović et al., 2009), which is calculated as

$$\boldsymbol{u}_c = C_\alpha|\boldsymbol{u}|\frac{\nabla\alpha}{|\nabla\alpha|} \tag{12}$$

where C_α is a user-defined variable determining the effect of the compression term and is set to 1 in this study to make the artificial compression term fully work. $\dfrac{\nabla\alpha}{|\nabla\alpha|}$ denotes the unit vector normal to the interface.

For the spatial discretization, the convection and diffusion terms in the momentum equation are respectively solved by using the linear upwind and linear corrected schemes (Greenshields, 2016), and the source terms are discretized with the same linearization as that in the work of Patankar (2018). The second and the third terms on the left-hand side of the phase volume fraction transport equation (11) are respectively discretized by the Gauss van Leer and the second-order linear differencing schemes. In addition, the PIMPLE algorithm (Greenshields, 2016), which is a combination of the pressure-implicit split operator (PISO) and the semi-implicit method for pressure-linked equations (SIMPLE) algorithms, is used to solve the pressure-velocity equation (Márquez Damián, 2010).

For the temporal discretization, the first-order Euler implicit scheme is employed. The adaptable time step technique is used to ensure the stability of the solution procedure based on the Courant number Co.

$$Co = \frac{|\boldsymbol{u}_{max}|\Delta t}{\Delta x} \tag{13}$$

where $\boldsymbol{u}_{max}$ is the maximum velocity in the whole computational domain, Δx is the minimum mesh size.

Using the values for $\boldsymbol{u}_{max}^0$ and Δt^0 from a previous time step, the maximum local Courant number Co^0 is calculated and thus a new time step can be evaluated by the following expression as:

$$\Delta t^n = \min\left\{\frac{Co_{max}}{Co^0}\Delta t^0, \left(1 + \lambda_1\frac{Co_{max}}{Co^0}\right)\Delta t^0, \lambda_2\Delta t^0, \Delta t_{max}\right\} \tag{14}$$

where $Co_{\max}$ and $\Delta t_{\max}$ are the maximum limit values for the Courant number and the time step, respectively. $\lambda_1 = 0.1$ and $\lambda_2 = 1.2$ are damping factors deployed to prevent oscillations during the time advancement. In this study, the setting of $\Delta t_{\max}$ can be arbitrary, as the time step can solely be adapted based on the setting of $Co_{\max} = 0.2$ as suggested by Berberović et al. (2009). At each time step, the PIMPLE algorithm solves the pressure equation and momentum corrector for 8 times (i.e., sub-cycles) with maximally 1000 iterations per sub-cycle to reach an order of 10^{-7} for the step residuals before advancing to the next time step.

2.3. *Mesh study and boundary conditions*

As mentioned above, grid resolution is one of the most important elements in determining the interface capturing quality by the VOF method. Accurate calculation of the phase volume fraction distribution is crucial for precise evaluation of the surface curvature of the interface in the air entrapment zone. To this end, a multi-block structured mesh topology is specially designed, as illustrated in FIGURE 3(a). An inner block (shown by the green dashed rectangle) is specified to encompass the air entrapment zone, where the smallest grid size is allocated uniformly to ensure the finest grid resolution for capturing the micrometric air film. In order to avoid the possible unfavorable effect of parasitic currents generated across the interface, a suboptimal block (the blue dashed rectangle) is extended from the upper-right ends of the air film block to surround the whole drop, with the grid sizes gradually growing outwards by up to a maximum factor of 2. Away from the drop block, an outmost block with the coarsest grid size is extended to comprise the whole computational domain of $4R \times 6R$. This meshing strategy enables an economic computational demand while being able to capture the entrapped air film with a high grid resolution, as shown by the red curve in FIGURE 3(b).

As shown in FIGURE 3(a), the no-slip wall condition ($u = 0$) is applied to the solid substrate and a fixed-value pressure is specified with the "pressureInletOutletVelocity" boundary condition for flow velocity across the "Atmosphere" boundaries. The contact line dynamics is one of the deterministic factors in drop-liquid impact research. For a closely relevant phenomenon of a solid sphere impacting a liquid pool surface, Duez et al. (2007) found that the air entrapment and the resulted splash can only be generated at a velocity above a threshold value depending on both the static contact angle and the capillary velocity (i.e. the ratio between surface tension and fluid viscosity). Li et al. (2015) observed fine azimuthal undulations at the first contact on the mica due to the contact line dynamics, without which the contraction of the air film into a spherical bubble would not occur to reduce the surface energy (Josserand and Thoroddsen, 2016). For smooth surfaces, the relationship between the velocity at the edge of the liquid-gas interface and the dynamic contact angle has been studied experimentally (Ralston et al., 2008). In the stationary status where a liquid front moves with constant (non-zero) velocity with respect to a solid surface, a single curve can be obtained between the contact angle and the capillary number Ca ($Ca = \mu_l V_0 / \sigma$) for different liquids. For smaller capillary numbers, the contact line moves under the Tanner's law or its variants. For larger capillary numbers, the contact line finally turns unstable (Boelens et al., 2018; Boelens and de Pablo, 2018, 2019; Latka et al., 2018). The dynamic contact line model implemented in OpenFOAM is defined as (Andersson et al., 2010):

$$\theta = \theta_0 + (\theta_a - \theta_r) \cdot \tanh\left(\frac{u_{wall}}{u_\theta}\right) \tag{15}$$

8

where θ, θ_0, θ_a and θ_r are the dynamic, static, advancing and receding contact angles, respectively. u_θ is the dynamic contact angle with a specified velocity scale. u_{wall} is the contact line moving velocity in parallel to the wall, which becomes a part of the solution when specifying the contact angle condition related to $\nabla\alpha$ at the contact line that is implicitly allowed to 'slip' in the local cell.

The mesh independence was examined by calculating the interface using the SLIC scheme with the inner block mesh refined by the law Level $i = 0.4/2^{i-1}$ µm, which implies that the Level-1 mesh has the coarsest grid size of 0.4 µm while the Level-5 mesh has the finest size of 0.025 µm for the air entrapment zone. FIGURE 5 shows the time evolution of the minimum air layer thickness h_{min}, which is one of the most sensitive quantities with the mesh size change, calculated with simulation results from the four-leveled meshes. Although small deviations can be observed between the different levels, a rapid convergence of the results is found for the Level-3 mesh, as the difference of the results between the Level-3 and the meshes with higher resolutions are not significant. Therefore, the Level-3 mesh (with a cell size of 0.1 µm) is adopted for all the remaining simulations. To validate the accuracy of the SLIC scheme for the current study, a special calculation of the air film with the PLIC scheme on the finest mesh was also performed. From Figure 5(b) it is also seen that the results obtained by both interface calculation methods do not exhibit significant difference between each other, validating that the undulations at the rim of the air film comes from the capillary waves rather than the SLIC interface reconstruction scheme.
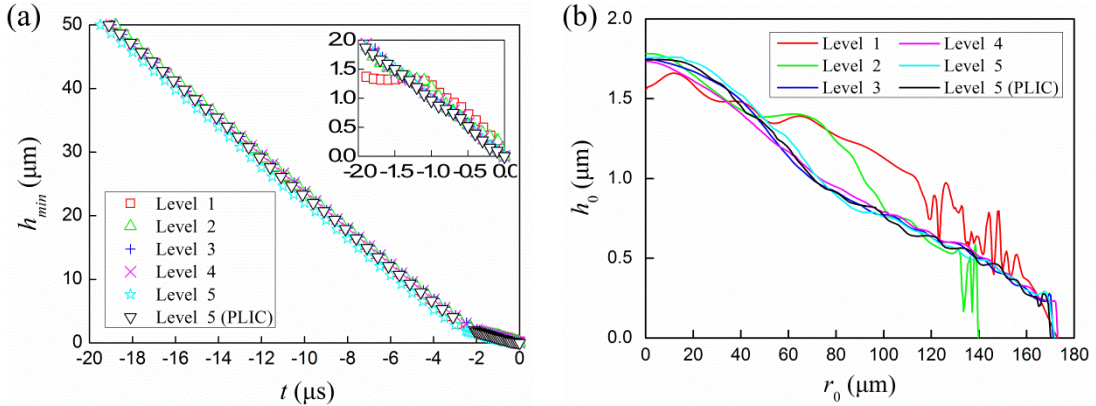

FIGURE 5. Mesh independence examination for the present study: (a) Time evolution of the minimum air layer thickness h_{min}, for different mesh resolutions (Level $i = 0.4/2^{i-1}$ μm) at $V_0 = 2.97$ m/s. The inserted sub-figure shows an enlarged view of the profiles during the air drainage period. (b) The profile of the air film upon contact simulated by the five levels of meshes. Both figures indicate that mesh-independent simulation results can be achieved from the Level-3 mesh on.

3. RESULTS AND DISCUSSION

3.1. Dimple before contact ($t \leq 0$)

FIGURE 6 shows the vertical coordinate $h(r,t)$ and radial coordinate $r(t)$ of the bottom of the liquid drop during free falling. While the drop is far away from the substrate, the pressure of air underneath the drop p_g due to viscous drainage scales as $p_g \Box \mu_g V_0 R / h^2$ (Mandre et al., 2009), which is smaller than the ambient pressure p_0. As the drop continues to fall down, p_g rises. At several microseconds prior to the drop-solid contact when the pressure of the underlying air becomes comparable to the ambient pressure, i.e. $p_g \Box p_0$, the

9

drop deforms to form a dimple on the drop-air interface, which is bounded by a kink at the outer edge. The time for the dimple formation is around t = -4.3 μs, -2.5 μs and -0.91 μs for the three impact velocities in FIGURE 6(a)-(c), respectively. The point of minimum separation between the droplet and substrate is decelerated by the air layer (Kolinski et al., 2012). For the $V_0 = 4.5\, m/s$, the drop velocity rapidly decelerates from 3.15 m/s at -1.35 μs to almost rest upon contact, implying a deceleration rate of $-2.33 \times 10^6\, m/s^2$, which is close to the experimental measurement under a similar impact condition (Li and Thoroddsen, 2015).

Note that the surface tension is initially unimportant compared to the much larger inertia of the drop, thus the pressure gradient of the compressed air accounts for the deceleration of the drop. However, the interfacial curvature diverges more quickly than the air pressure, leading to an enhancement of surface tension effect in the proximity to the substrate. In most of previous experimental studies, the interface was imagined to be a smooth gaseous surface, which is valid when surface tension is weak. With sufficient temporal resolution available in the present simulations, it is seen that the dimple surface is actually undulant due to the enhancement effect of surface tension near contact, as shown in FIGURE 6(d), which is similar to that observed by experiments (de Ruiter et al., 2015) as well as the solutions based on the lubrication theory (Duchemin and Josserand, 2011; Hicks and Purvis, 2010, 2013).. As can be discerned from a careful inspection of the motion, the center of the dimple rises rapidly near the contact instant, as shown in FIGURE 6(e). This rapid expansion remains for a while even after contact, as observed experimentally by Li and Thoroddsen (2015). The phenomenon of central air layer expansion is resulted from the high lubrication pressure in the region beneath the drop, producing a cushioning effect on the drop above. The evolution of the central air film thickness $h(r=0)$ as a function of time t till contact is plotted in FIGURE 6(f). Increasing V_0 renders a smaller air film thickness upon touchdown ($t=0$), as larger impact velocity means smaller Stokes number St and the higher inertial pressure force of the drop balancing the cushioning effect of the compressed air.
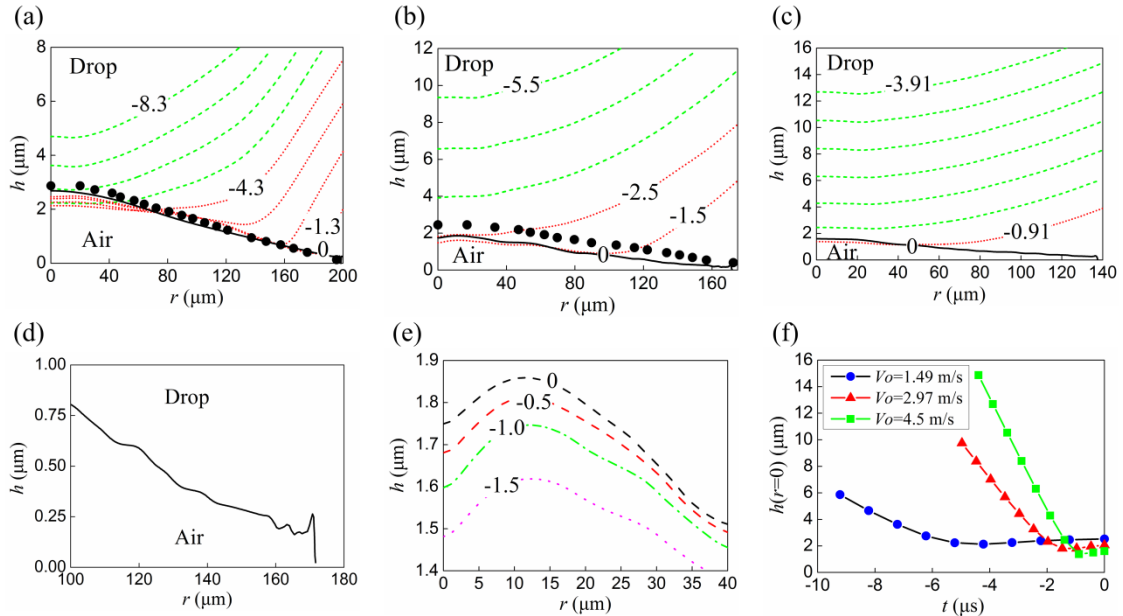

FIGURE 6. The deformation of the bottom of the water drop at impact velocities of (a) V_0 = 1.49 m/s, (b) V_0 = 2.97 m/s, (c) V_0 = 4.5 m/s, respectively. Dashed lines: unchanged shape during drop falling, dotted lines: air layer with a dimple, solid lines: air layer upon contact (t = 0 μs). The available experimental data are also shown by solid black circles. The solid surface is located at the zero axial coordinate. The labels on the curves show the time instants in the unit of μs while the unlabeled curves

are uniformly spaced. (d) Undulations present on the air film upon contact at $V_0 = 2.97$ m/s, (e) Rapid rise of the center of the air film before contact at $V_0 = 2.97$ m/s, (f) Time history of the air film thickness at the center of the film $h(r = 0)$ at different impact speeds.

The time histories of pressure on the air-water interface are plotted in FIGURE 7. At the initial stage of the impact, the pressure generally decreases towards the rim of the dimple, as there is no significant change in the curvature of the interface (green-colour curves in FIGURE 7(a)), and the pressure almost equals to the ambient air pressure, as shown in FIGURE 7(b). Subsequently, the pressure at the center gradually increases to be just above the ambient pressure of 1 *atm* to balance the inertia of the drop. When the interface curvature changes to generate a dimple at the interface, the pressure begins to rise from the center and reaches the peak at the kink (red-colour curves in FIGURE 7(a)). This trend continues till the contact between the drop and substrate. Upon contact, the pressure reaches the highest at the contacting point and progressively recovers in the later retraction phase. These noticeable features are found in consistency with the three-dimensional results obtained by the boundary-integral method (Hicks and Purvis, 2010). Also it can be seen from FIGURE 7(b) that the maximum pressure on the interface increases rapidly from about 4 μs before contact, reaches the maximum upon contact, and recovers at about 4 μs after contact. The maximum pressure is almost linearly proportional to the impact velocity, as shown later in FIGURE 10(b).
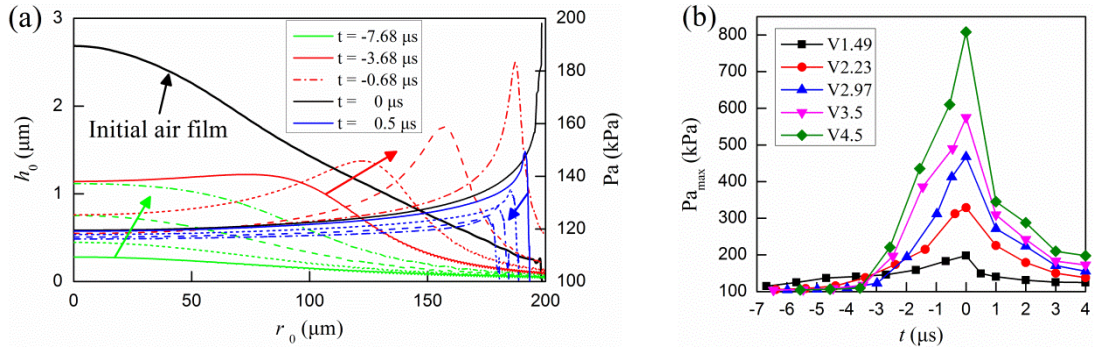

FIGURE 7. (a) Evolution of the pressure on the water-air interface for drop impact at $V_0 = 1.49$ m/s. The colorful arrows point out the temporal sequence movements. Green lines: pressure profiles with no dimple present on the interface, red lines: with dimples, black lines: upon the contact, blue lines: after the contact. The unlabeled curves are uniformly spaced in time. (b) Time histories of the maximum pressure on the air film layer for all the impact velocities of interest in this study.

3.2. Kink before contact ($t \leq 0$)

FIGURE 8(a) and 8(b) depict the axial and radial trajectories of the kink as a function of time, respectively. Both of the trajectories show approximately linear correlations with time, indicating that the axial velocity V_k and radial velocity U_k of the kink are nearly constant during a short time period prior to contact. Through linear curve fitting, the two normalized velocities as a function of impact velocity are obtained, as shown in FIGURE 8(c) and 8(d), respectively. It is indicated that the axial velocity V_k is of one order lower while the radial velocity U_k is of one order higher than the impact velocity in magnitude. Comparing with the maximum radial velocity $U_k = 132.5\,m/s$, the maximum axial velocity is only $V_k = 1.5\,m/s$ at $V_0 = 4.5\,m/s$. Jian et al. (2018) proposed an assumption that $\partial_t h_k \square 1$, namely, V_k has a linear correlation with V_0. Here, the assumption above is

manifested with the factors of 0.36 and 35.1 for the axial and radial velocities, respectively.

By assuming that the drop contacts with the solid surface in a finite time along with the advection of the air radially inside the drop and neglecting the inertia of the air, the full Navier-Stokes equations can be simplified to the lubrication equation (Mandre et al., 2009). A self-similar solution of the simplified equation yields the following scaling for V_k and U_k (Li and Thoroddsen, 2015):

$$V_k / V_0 \square\ St^0 \ , \quad U_k / V_0 \square\ St^{-1/3} \tag{16}$$

The data in the inserted sub-figures in FIGURE 8(c) and 8(d) shows good correspondence with the above scaling with two pre-factors of 0.31 and 0.39, respectively. Mandre and Brenner (2012) and Li and Thoroddsen (2015) showed the same power law for U_k with two pre-factors of 0.34 and 0.42, respectively.
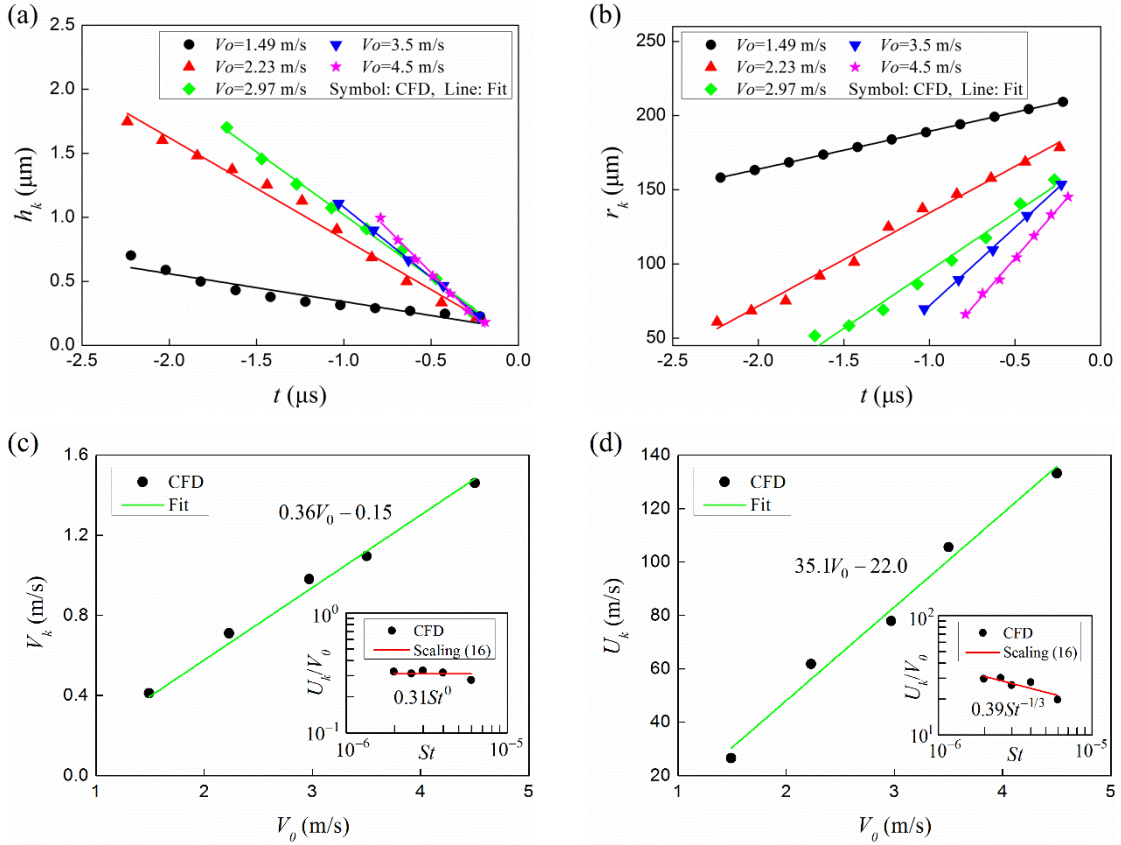

FIGURE 8. Kinematics of the kink during the touchdown phase. (a) time history of the height h_k and (b) the radius r_k. (c) the axial velocity V_k and (d) the radial velocity scale U_k as a function of the impact velocity. The best linear fitted results are shown by the solid green line. The CFD results are also compared with the scaling law of equation (16) in the subfigures.

3.3. Air film upon contact ($t = 0$)

Prior to contact, the kink expands radially outwards and approaches towards the substrate simultaneously under the balance between the lubrication pressure in the air trying to escape the oncoming drop and the inertial pressure of the drop trying to entrap the air inside (Korobkin et al., 2008; Mandre et al., 2009; Mani et al., 2010). This process is repeated even at smaller distances until the contact is made and a thin air film is entrapped. The pressure in the entrapped gas p_g and the inertial pressure in the liquid p_l can be derived and are respectively written as follows (Mandre et al., 2009):

$$p_g \sim \frac{\mu_g V_0 R}{h^2} \sim \frac{St}{h^2} \ , \quad p_l \sim \rho_l V_0^2 \sqrt{\frac{R}{h}} \sim \frac{1}{\sqrt{h}} \tag{17}$$

Balancing the two pressures above and using the simple geometric arguments for the radius of the air film $r = \sqrt{Rh}$, the scaling laws of the height h_0 and radius r_0 of the initial air film can respectively be obtained in relation to the St number as

$$h_0 / R \propto St^{2/3} \ \text{ and } \ r_0 / R \propto St^{1/3} \tag{18}$$

FIGURE 9 shows the results of the thickness and radius of the initial air film obtained by the above scaling laws. It is worth noting that both (Liu et al., 2013) and the present study assume that the drop remains spherical upon contact with the solid. Li and Thoroddsen (2015) took the factor of droplet deformation due to its oscillation during free falling into consideration and measured the radius of curvature at the bottom of the drop R_b at the onset of cushioning. In order to evaluate the influence of drop oscillation on the agreement between available test results and the scaling law, we also calculate three cases of $R_b = 3.2, 4.1, 8.2$ mm and $V_0 = 4.05, 1.06, 2.43$ m/s respectively, with the equivalent spherical drop radius of 2.6 mm for all the three cases (Li and Thoroddsen, 2015). The results are shown in FIGURE 9 as well. Due to the difficulty of acquiring the accurate shape of the oscillating drop from Li and Thoroddsen's experiment, here we adopted a quasi-reference method by setting $R = R_b$ for a spherical drop upon contact in the simulation based on the self-similarity property of the scaling law. It is seen that the current CFD results can well be scaled by the scaling law of equation (18), with the pre-factors of 4.57 and 6.28, respectively. A much better agreement with the scaling law is obtained by scaling with the radius of curvature at the bottom of the drop under moderate oscillation conditions associated with a much higher video frame rate used in the experiment of Li and Thoroddsen (2015). However, it is also seen that as R_b increases to the highest value of $R_b = 8.2\,mm$ (i.e. $S_t = 9.2 \times 10^{-7}$), h_0 significantly deviates from the scaling law (i.e. the blue point at the left bottom of FIGURE 9(a)). In this case, the oscillation of the drop is quite intense with the dynamic effect rapidly transferred to the thickness of the air bubble due to the short distance to the solid surface while gradually dissipated within the long distance of the spreading kink.
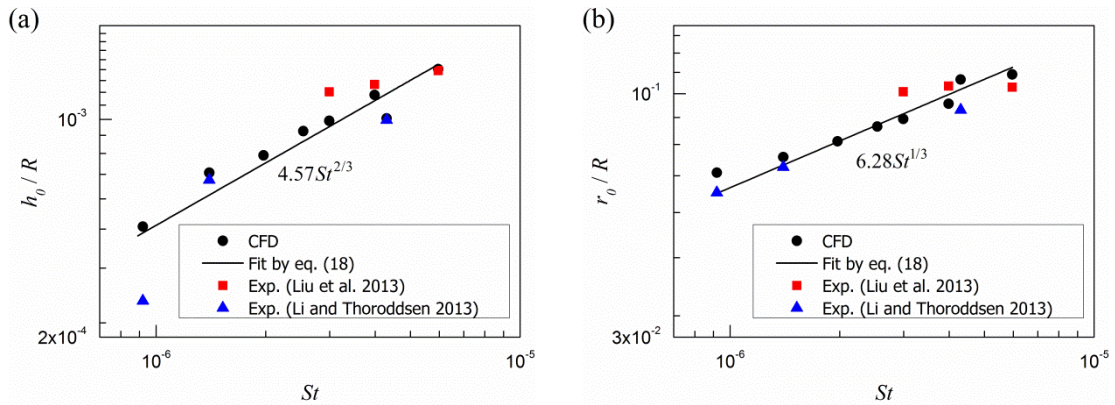

FIGURE 9. The dimensionless (a) central height and (b) radius of the initial air film plotted with the Stokes number in logarithmic scales. The results fitted by equation (18) with the CFD data and the experimental data from (Liu et al., 2013) and (Li and Thoroddsen, 2015) are associated.

FIGURE 10(a) shows the instantaneous pressure field around the air film upon the liquid-solid contact for

$V_0 = 2.97$ m/s. As the drop attempts to contact with the solid surface, there is a rapid increase in the air pressure towards the rim of the air film (Mandre et al., 2009; Mani et al., 2010). The dynamics of this pressure rise are important to understanding the underlying physical mechanism behind the droplet splashing (Aboud et al., 2020; Mandre and Brenner, 2012; Riboux and Gordillo, 2014), despite that splashing is not the primary topic of this study. FIGURE 10(a) clearly indicates that the pressure on the initial air film has an analogously parabolic increase from the center towards the rim, rather than a uniform distribution. The average pressure in the air film p_g is overall much higher than the ambient pressure $p_0 = 1$ atm in such a small compressed region. By setting $r_0 = \sqrt{Rh_0}$ in equation (17), p_g can be obtained and written as

$$p_g = p_0 + C_1 \rho_l V_0^2 r_0 / h_0 \tag{19}$$

For water, the pre-factor $C_1 = 0.33$ can be obtained through data fitting.

According to (Mandre et al., 2009), the maximum pressure p_{max} can be expressed using the parameters defined in the present study as

$$p_{max} = C_2 \frac{\mu_0 V_0}{RSt} \left(\frac{RU_k^3}{h_0} \right)^{1/2} + C_0 \tag{20}$$

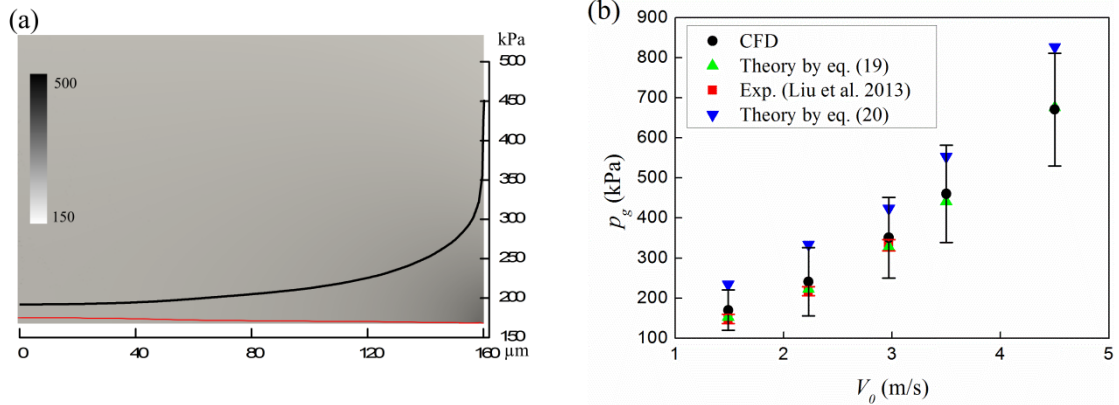where C_0 and C_2 are the two fitting coefficients.

FIGURE 10. (a) Pressure contour near the initial air film for the drop impact at $V_0 = 2.97$ m/s. The red curve shows the profile of the initial air film as well as the black curve the radial pressure distribution on the air film. (b) The pressure distribution on the initial air film for all the impact cases of interest. The solid black circles represent the average value of the CFD predictions with the error bars denoting the minimum pressure p_{min} at the center and the maximum pressure p_{max} at the rim of the air film, The green triangles, red squares and line denote the experimental measurements (Liu et al., 2013), theoretical estimations by equation (19) and the scaling law in equation (20), respectively.

FIGURE 10(b) plots the pressure in the initial air film obtained by the current CFD simulation, the experiment (Liu et al., 2013), the theoretical analysis in equation (19) and scaling equation (20) of p_{max} at all the impact velocities. The mean values between the pressure at the center (i.e. lower limit) and the pressure at the rim (i.e. upper limit) obtained by CFD agree well with the experimental measurements and the theoretical estimates. The numerical predicted maximum pressure p_{max} is also in good agreement with the scaling law in equation (20), with the coefficients $C_0 = 299.66$ and $C_2 = 0.00048$. Meanwhile, the CFD results generally show

the same trend as the experimental measurements and the theoretical estimations, i.e. at small impact velocity V_0, p_g approaches the ambient air pressure p_0 and rises rapidly along with the increase of V_0. Liu et al. (2013) attributed this to the large geometric factor r_0/h_0. Indeed, it is obtained that $r_0/h_0 = 71\square 86$ from the present simulations and $r_0/h_0 = 60\square 82$ from the experiment (Liu et al., 2013), both of which do not present such large difference as that occurs on p_g. The rapid rise of pressure in the initial air film should be more attributed to the impact velocity since it has a square multiple effect on the growth of p_g.

3.4. Air film after contact ($t > 0$)

The detailed evolution process of the air film requires further clarification. Here, the parameters characterizing the evolutionary shape, i.e., the size of the base $\lambda(t)$, the height $\delta(t)$ of the rim and the radial extent of the film $L(t)$ shown in FIGURE 1(b) are measured and plotted as a function of time in FIGURE 11(a) to 11(c), respectively. From the almost overlapping curves within approximately the first 25 μs, it can be seen that the size and height of the rim base do not show significant difference between the different impact velocities during the retraction phase. As the crest of the capillary wave touches the substrate, $\lambda(t)$ experiences a rapid increase till the maximum point. The thickening trend of the rim is almost identical to that behaves in the experiment by Liu et al. (2013), and the magnitude of the maximum $\lambda(t)$ is of the same order but a slightly larger than Liu et al.'s experimental results. This is mainly because the thick rim calculated in this study is not an ideally hemispheric shape which was assumed in Liu et al.'s experiment.

Following this, the toroidal air bubble is formed, contracted and detached from the substrate (i.e. represented by the open symbols). Furthermore, it also can be seen that there is a noticeable increase in the axial acceleration during the contraction phase (see, e.g. FIGURE 11(b)). Thoroddsen et al. (2005) suggested a formulation to estimate an instantaneous radius of the air film after contact, which is expressed as

$$L = r_0 \exp(-C\sqrt{\pi\sigma/(\rho_l V_{bubble})}\, t) \tag{21}$$

where r_0 is the radius of the air film upon contact. V_{bubble} is the volume of the final spherical air bubble and hereby in this paper it can be calculated from the bubble diameter which is plotted in FIGURE 11(d). C is a proportionality constant.

It is seen from FIGURE 11(c) that the simulated results of the radius are in good agreement with the theoretical results by equation (21) till the end of the retraction phase, except for a small deviation by approximately the same order of magnitude at the beginning (i.e., the solid symbols). From the contraction phase when the toroid is formed, the results begin to deviate from the theoretical values (i.e., the empty symbols), implying an increase in the radial acceleration of the bubble compared to that in the retraction phase. The above finding reveals a differential characteristic between the retraction and contraction phases which were not distinguished previously (Thoroddsen et al., 2005).

As already described above, the daughter droplet is pinched off after contraction and a spherical air bubble is formed. According to a previous study (Thoroddsen et al., 2005), a relation $h_0 = V_b/(\pi r_0^2)$ can be obtained, in which V_b is the total volume of the air bubble. Associating equation (18) with equation (21), a relationship

between the diameter of the final air bubble D_b and the impact velocity V_0 can be derived as

$$D_b \sim V_0^{-4/9} \tag{22}$$

FIGURE 11(d) depicts the best fitted results by the scaling law of equation (22), for which both the trend and magnitude are generally in good agreement with that by present direct numerical simulations. On the other hand, within the range of impact conditions of interest in this paper, increasing the impact speed will result in smaller air bubbles eventually. In addition, it is also found that the pressure in the final air bubble is much lower than that in the initial air film. For example, the mean pressure in the initial air film is about 670.6 kPa for $V_0 = 4.5\,m/s$ (see FIGURE 10). However, it decreases to 133.7 kPa in the final spherical air bubble, suggesting that the air evolution is overall a decompression process.
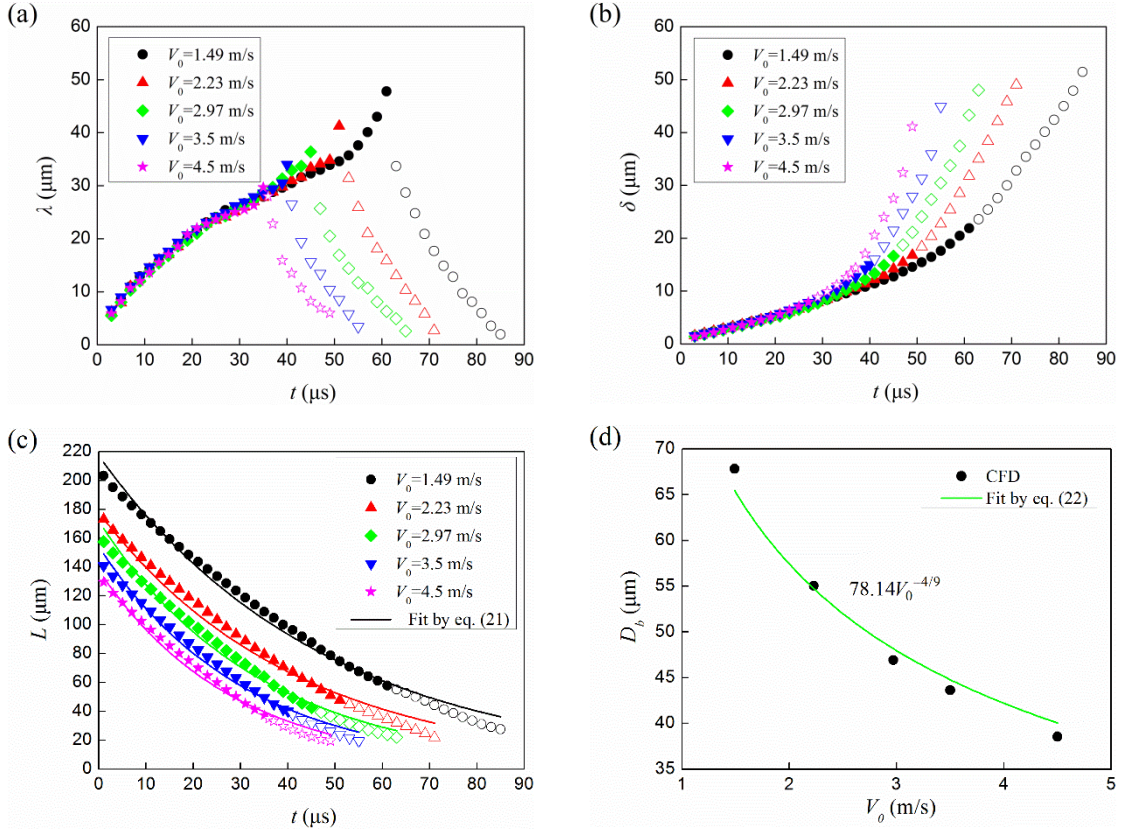

FIGURE 11. Evolution of the entrapped air in the retraction and contraction phases. (a) The length $\lambda(t)$ and (b) height $\delta(t)$ of the rim, (c) the radial extent $L(t)$ of the air film. The values from the time instant when the toroidal air bubble is formed are represented by open symbols. For $L(t)$, the fitted results using equation (21) are also shown. (d) Values of the final air bubble diameter directly from current CFD simulation and by using the scaling law of equation (22).

In order to more precisely discern between the retraction and contraction phases, the transition point and time span of each phase need to be determined quantitatively. Here, the retraction is defined to start immediately after contact and end right before a full capillary wave is formed at the center, followed by the contraction starting and ending as soon as the top of the toroidal bubble is coalesced. The time periods of the retraction phase T_{rt} and of the contraction phase T_{ct} are obtained and shown in FIGURE 12(a). Both periods decrease monotonously with the impact speed in linear relationship shown in FIGURE 12(a). Having determined the time periods for each phase, it would be straightforward to further calculate the average values of the retraction and contraction speeds.

The mean retraction speed is about twice of the mean contraction speed and neither has significant dependence on the impact speed, as shown in FIGURE 12(b).
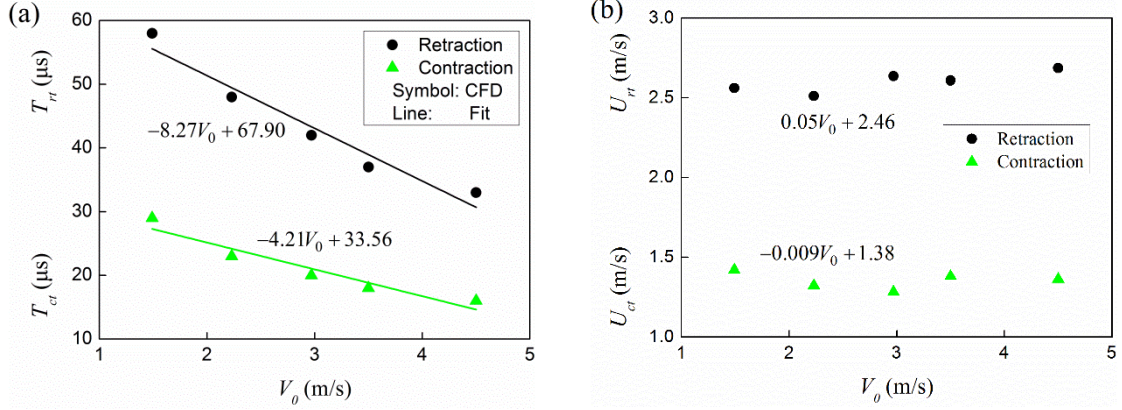

FIGURE 12. Kinematics of the air bubble in the retraction and contraction phases. (a) The retraction time period T_{rt} and the contraction time period T_{ct}. (b) The mean retraction velocity U_{rt} and contraction velocity U_{ct} for all impact speeds studied. The symbols denote the values directly obtained from the current CFD simulations while the solid lines represent the best linear fitting results.

3.5. Vortex ring accompanying shape evolution

The phenomenon of vortex generation and formation of a vortex ring has been observed when a liquid drop impinges on a liquid pool (Behera et al., 2019; Jian et al., 2020a; Thoraval et al., 2012). Here, we will show that the air entrapment process can also be dictated by the vorticity generated at the free surface during the impact of the drop onto the substrate. The strength of vorticity for a stationary two-dimensional free surface is defined as:

$$\Delta\omega = \frac{2q}{R_c} \tag{23}$$

where $\Delta\omega$ is the vorticity produced by flow circulation q within a local radius of curvature R_c. It can be seen from equation (23) that the variation of the air-water interface curvature accounts for the generation, change in the strength and dynamics of the vortex ring. FIGURE 13 shows the interaction between the vortex ring and the air-water interface in the evolution process. At the beginning of the retraction phase, a core vortex emerges at the high-curvature rim of the air film and gradually moves towards the center together with the air film. Meanwhile, another smaller vortex is also generated at the trough of the capillary wave generated during the retraction of the air film, which magnifies along with the core vortex. In the contraction phase, the core vortex is gradually pinched towards the right position relative to the air bubble due to the coalescence at the top of the toroidal bubble. Besides, the smaller vortex at the trough of the capillary wave undergoes a series of splitting and coalescence. As the air bubble moves upwards in the pinch-off phase, the core vortex is further pinched downwards relatively to the bottom of the drop. During pinch-off, a secondary local vortex emerges at the rugged curvature position of the interface, further smoothing the local surface of the air bubble. All above manifests that the generation and evolution of these vortex rings are closely related to the deformation of the water-air interface, implying some physical mechanisms between both that have not been realized previously. On the other hand, it can be seen from the whole process that the core vortex ring is at the periphery of the air film/bubble, while its core is always located in the liquid domain, indicating that the core vortex is originated from the liquid phase. Therefore, according to

17

the principle of force interaction, the core vortex ring shall in turn push the evolution of the air film/bubble. Meanwhile, the smaller vortex rings will assist the core vortex to smooth the local regions and promote the evolution of the entrapped air into a spherical bubble as well. Recently, Jian et al. (2020b) also discovered the phenomenon of vortex shedding during the contraction of a air sheet in a surrounding liquid via two-dimensional CFD simulations. From both of their and the present studies, it is reasonable to speculate that the vortex shall play an import role in the evolution of air entrapment, although further studies are needed to understand the effect of the vortex rings if they were absent.
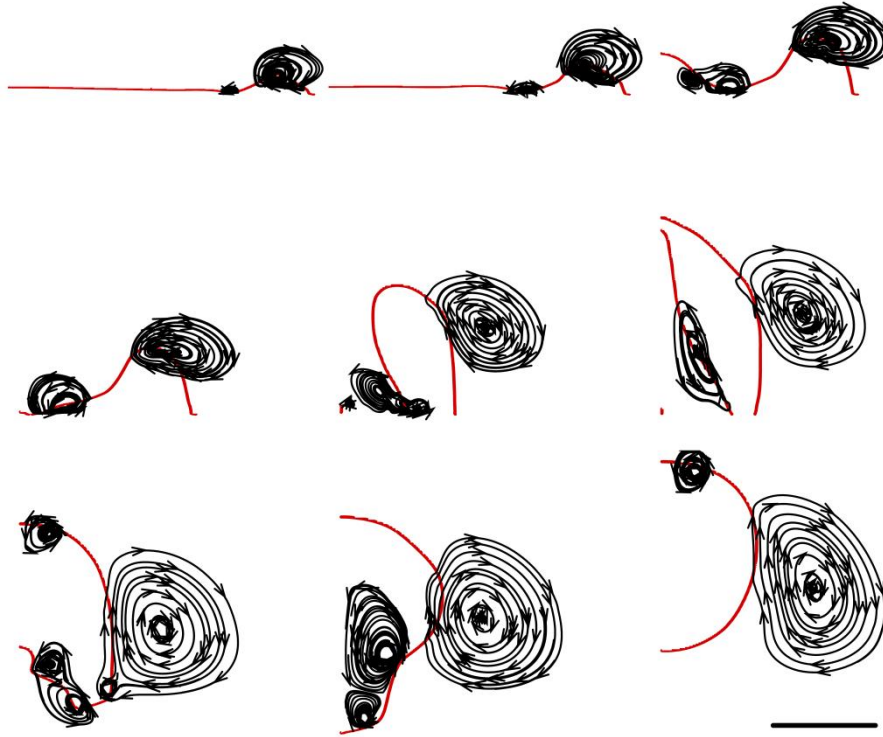
FIGURE 13. The shape of the entrapped air film/bubble (red lines) and the surrounding streamlines (black lines with arrows indicating the direction) showing the formation and propagation of the vortex ring within the various evolution phases of the entrapped air at impact velocity $V_0 = 2.97$ *m/s*. The profiles from left to right in the upper row (i.e. the retraction phase): 20 μs, 30 μs, and 42 μs; in the middle row (i.e. the contraction phase): 45 μs, 56 μs, and 62 μs; in the bottom row (i.e. the pinch-off phase): 68 μs, 74 μs, and 96 μs, respectively. The length of the scale bar on the bottom right is 25 μm.

The values of the radial and axial displacements of the core vortex are presented in FIGURE 14. It can be obtained that the core vortex gradually moves inwards at an almost uniform radial speed of 2.63 *m/s* (i.e. the slope shown in FIGURE 14(a)) till the end of the retraction phase, which is close to the radial speed of the core vortex ring ($U_{rt} = 2.64$) shown in FIGURE 12(b), indicating a synchronization of both evolutions of the entrapped air and the core vortex ring. Simultaneously, the core vortex slowly moves upwards at a small axial speed of 0.42 *m/s* (i.e. the slope shown in FIGURE 14(b)). The quite good regularity exhibiting on the kinetics of the core vortex ring further validates the accuracy of the numerical simulation approach in the present study.
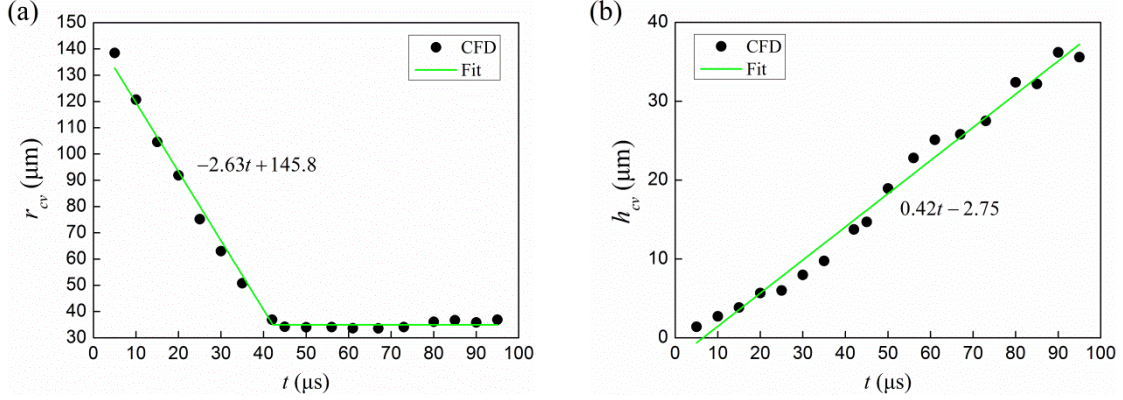
FIGURE 14. Time history of (a) the radial displacement r_{cv} and (b) the axial displacement h_{cv} of the core vortex ring during the whole air evolution process for the impact speed $V_0 = 2.97$ *m/s*. The solid green lines denote the best linear fitting results.

4. CONCLUSION

In this study, a direct numerical simulation of the whole evolution process of the air entrapment occurring in a water drop impact on a dry smooth solid surface is performed. It is found that as the drop is released from a certain height above the substrate, the air in the region beneath the drop is continuously compressed, resulting in the formation of a dimple bounded by a kink at the outer edge at a time-scale of microseconds prior to the liquid-solid contact. The dimple and the kink descend to approach the substrate. As the kink contacts the solid surface, a thin air film is entrapped beneath the drop. The air film retracts towards the center under the balance between the surface tension and the inertial forces, contracts to a hatted toroid with a daughter droplet beneath to minimize the surface energy from the capillary waves developed during the retraction phase, and finally turns into a spherical air bubble at the center after a pinch-off process. Detailed quantitative characterizations of each phase described above have been presented and discussed in detail. Lastly, it is shown that the shape of the air film induces a core vortex ring together with some smaller vortex rings intermittently, which develops synchronously with the air film. The core vortex ring pushes the evolution of the overall shape and the smaller vortex rings smooth the local regions of the air film/bubble, promoting the evolution of the air entrapment.

The results and findings in this research can further be extended to more scaling analyses in the future. Meanwhile, the present numerical method also allows identifying the influence of the air by varying its density and viscosity. Recent experimental measurements by Li et al. (Li et al., 2018) have revealed a string of teeth-like undulations which can cause uneven vortex-induced ejecta around the periphery in the azimuthal direction in liquid-liquid impacts at relatively large *Re* and *We*, breaking the assumption of axisymmetry that is commonly adopted by many researchers in the field. Although there are no such researches in the liquid-solid impact scenario, three-dimensional simulations are necessary in the future to confirm the azimuthal evolution of the air entrapment and the role of the accompanying vortex structures in the process.

scrutiny of the language.

REFERENCES

https://cfd.direct/openfoam/free-software/multiphase-interface-capturing/.

Aboud, D.G.K., Wood, M.J., Kietzig, A.M., 2020. Influence of liquid properties on the oblique splashing threshold of drops. Physics of Fluids 32, 061402.

Andersson, P., Andric, J., Rynell, A., 2010. Tutorial multiphaseInterFoam.

Behera, M.R., Dasgupta, A., Chakraborty, S., 2019. On the generation of vorticity and hydrodynamics of vortex ring during liquid drop impingement. Physics of Fluids 31, 082108.

Berberović, E., van Hinsberg, N.P., Jakirlić, S., Roisman, I.V., Tropea, C., 2009. Drop impact onto a liquid layer of finite thickness: Dynamics of the cavity evolution. Physical Review E 79, 036306.

Boelens, A., Latka, A., de Pablo, J., 2018. Observation of the pressure effect in simulations of droplets splashing on a dry surface. Physical Review Fluids 3, 063602.

Boelens, A.M., de Pablo, J.J., 2018. Simulations of splashing high and low viscosity droplets. Physics of Fluids 30, 072106.

Boelens, A.M., de Pablo, J.J., 2019. Generalised Navier boundary condition for a volume of fluid approach using a finite-volume method. Physics of Fluids 31, 021203.

Bouwhuis, W., van der Veen, R.C., Tran, T., Keij, D.L., Winkels, K.G., Peters, I.R., van der Meer, D., Sun, C., Snoeijer, J.H., Lohse, D., 2012. Maximal air bubble entrainment at liquid-drop impact. Physical Review Letters 109, 264501.

Brackbill, J.U., Kothe, D.B., Zemach, C., 1992. A continuum method for modeling surface tension. Journal of Computational Physics 100, 335-354.

Chandra, S., Avedisian, C., 1991. On the collision of a droplet with a solid surface. Proceedings of the Royal Society of London. Series A: Mathematical and Physical Sciences 432, 13-41.

Daly, B.J., 1969. A technique for including surface tension effects in hydrodynamic calculations. Journal of Computational Physics 4, 97-117.

de Ruiter, J., Lagraauw, R., Van Den Ende, D., Mugele, F., 2015. Wettability-independent bouncing on flat surfaces mediated by thin air films. Nature Physics 11, 48-53.

Duchemin, L., Josserand, C., 2011. Curvature singularity and film-skating during drop impact. Physics of Fluids 23, 091701.

Duez, C., Ybert, C., Clanet, C., Bocquet, L., 2007. Making a splash with water repellency. Nature Physics 3, 180-183.

Esmailizadeh, L., Mesler, R., 1986. Bubble entrainment with drops. Journal of Colloid and Interface Science 110, 561-574.

Gargi, K., Nilamani, S., Purbarun, D., 2019. Phenomenology of droplet collision hydrodynamics on wetting and non-wetting spheres. Physics of Fluids 31, 072003.

Greenshields, C., 2016. OpenFOAM User Guide Version 4.0. OpenFOAM Foundation Ltd., London.

Harlow, F.H., Welch, J.E., 1965. Numerical calculation of time‐dependent viscous incompressible flow of fluid with free surface. Physics of Fluids 8, 2182-2189.

Hemida, H., 2008. OpenFOAM tutorial: Free surface tutorial using interFoam and rasInterFoam. Chalmers University of Technology, Gothenburg.

Hicks, P., Ermanyuk, E., Gavrilov, N., Purvis, R., 2012. Air trapping at impact of a rigid sphere onto a liquid. Journal of Fluid Mechanics 695, 310-320.

Hicks, P.D., Purvis, R., 2010. Air cushioning and bubble entrapment in three-dimensional droplet impacts. Journal of Fluid Mechanics 649, 135-163.

Hicks, P.D., Purvis, R., 2013. Liquid–solid impacts with compressible gas cushioning. Journal of Fluid Mechanics 735, 120-149.

Hirt, C.W., Nichols, B.D., 1981. Volume of fluid (VOF) method for the dynamics of free boundaries. Journal of Computational Physics 39, 201-225.

Jian, Z., Channa, M.A., Kherbeche, A., Chizari, H., Thoroddsen, S.T., Thoraval, M.J., 2020a. To Split or Not to Split: Dynamics of an Air Disk Formed under a Drop Impacting on a Pool. Physical Review Letters 124, 184501.

Jian, Z., Deng, P., Thoraval, M.-J., 2020b. Air sheet contraction. Journal of Fluid Mechanics 899, A7-1-23.

Jian, Z., Josserand, C., Popinet, S., Ray, P., Zaleski, S., 2018. Two mechanisms of droplet splashing on a solid substrate. Journal of Fluid Mechanics 835, 1065-1086.

Josserand, C., Thoroddsen, S.T., 2016. Drop impact on a solid surface. Annual Review of Fluid Mechanics 48, 365-391.

Kolinski, J.M., Rubinstein, S.M., Mandre, S., Brenner, M.P., Weitz, D.A., Mahadevan, L., 2012. Skating on a film of air: drops impacting on a surface. Physical Review Letters 108, 074503.

Korobkin, A., Ellis, A., Smith, F., 2008. Trapping of air in impact between a body and shallow water. Journal of Fluid Mechanics 611, 365-394.

Latka, A., Boelens, A.M., Nagel, S.R., de Pablo, J.J., 2018. Drop splashing is independent of substrate wetting. Physics of Fluids 30, 022105.

Lee, J.S., Weon, B.M., Je, J.H., Fezzaa, K., 2012. How does an air film evolve into a bubble during drop impact? Physical Review Letters 109, 204501.

Li, E., Thoraval, M.-J., Marston, J., Thoroddsen, S.T., 2018. Early azimuthal instability during drop impact. Journal of Fluid Mechanics 848, 821-835.

Li, E., Thoroddsen, S.T., 2015. Time-resolved imaging of a compressible air disc under a drop impacting on a solid surface. Journal of Fluid Mechanics 780, 636-648.

Li, E., Vakarelski, I.U., Thoroddsen, S.T., 2015. Probing the nanoscale: the first contact of an impacting drop. Journal of Fluid Mechanics 785, 1-12.

Li, E.Q., Langley, K.R., Tian, Y.S., Hicks, P.D., Thoroddsen, S.T., 2017. Double contact during drop impact on a solid under reduced air pressure. Physical Review Letters 119, 214502.

Liu, Y., Tan, P., Xu, L., 2013. Compressible air entrapment in high-speed drop impacts on solid surfaces. Journal of Fluid Mechanics 716, 1-12.

Mandre, S., Brenner, M.P., 2012. The mechanism of a splash on a dry solid surface. Journal of Fluid Mechanics 690, 148-172.

Mandre, S., Mani, M., Brenner, M.P., 2009. Precursors to splashing of liquid droplets on a solid surface. Physical Review Letters 102, 134502.

Mani, M., Mandre, S., Brenner, M.P., 2010. Events before droplet splashing on a solid surface. Journal of Fluid Mechanics 647, 163-185.

Márquez Damián, S., 2010. Description and utilization of interFoam multiphase solver. FinalWork, Computational Fluid Dynamics–Facultad de Ingeniería y Ciencias Hidricas, UNL.

Mehdi-Nejad, V., Mostaghimi, J., Chandra, S., 2003. Air bubble entrapment under an impacting droplet. Physics of Fluids 15, 173-183.

Nguyen, V.B., Do, Q.V., Pham, V.S., 2020. An OpenFOAM solver for multiphase and turbulent flow. Physics of Fluids 32, 043303.

Nichols, B., Hirt, C., 1973. Calculating three-dimensional free surface flows in the vicinity of submerged and exposed structures. Journal of Computational Physics 12, 234-246.

Noh, W.F., Woodward, P., 1976. SLIC (Simple Line Interface Calculation), Fifthe International Conference on Numerical Methods in Fluid Dynamics, Enschede, The Netherlands.

Oishi, C.M., Thompson, R.L., Martins, F.P., 2019. Impact of capillary drops of complex fluids on a solid surface. Physics of Fluids 31, 123109.

Osher, S., Sethian, J.A., 1988. Fronts propagating with curvature-dependent speed: algorithms based on Hamilton-Jacobi formulations. Journal of Computational Physics 79, 12-49.

Patankar, S., 2018. Numerical heat transfer and fluid flow. Taylor & Francis.

Popinet, S., 2018. Numerical models of surface tension. Annual Review of Fluid Mechanics 50, 49-75.

Pumphrey, H.C., Elmore, P.A., 1990. The entrainment of bubbles by drop impacts. Journal of Fluid Mechanics 220, 539-567.

Ralston, J., Popescu, M., Sedev, R., 2008. Dynamics of wetting from an experimental point of view. Annual Review of Materials Research 38, 23-43.

Riboux, G., Gordillo, J.M., 2014. Experiments of Drops Impacting a Smooth Solid Surface: A Model of the Critical Impact Speed for Drop Splashing. Physical Review Letters 113, 024507.

Rioboo, R., Marengo, M., Tropea, C., 2002. Time evolution of liquid drop impact onto solid, dry surfaces. Experiments in Fluids 33, 112-124.

Schroll, R.D., Josserand, C., Zaleski, S., Zhang, W.W., 2010. Impact of a viscous liquid drop. Physical Review Letters 104, 034504.

Sigler, J., Mesler, R., 1990. The behavior of the gas film formed upon drop impact with a liquid surface. Journal of Colloid and Interface Science 134, 459-474.

Thoraval, M.J., Takehara, K., Etoh, T.G., Popinet, S., Ray, P., Josserand, C., Zaleski, S., Thoroddsen, S.T., 2012. von Karman Vortex Street within an Impacting Drop. Physical Review Letters 108, 264506.

Thoroddsen, S., Etoh, T., Takehara, K., Ootsuka, N., Hatsuki, Y., 2005. The air bubble entrapped under a drop impacting on a solid surface. Journal of Fluid Mechanics 545, 203-212.

Weller, H.G., 2008. A new approach to VOF-based interface capturing methods for incompressible and compressible flow. Technical Report TR/HGW/04 4.

Worthington, A.M., 1877. On the forms assumed by drops of liquids falling vertically on a horizontal plate. Proceedings of the Royal Society of London 25, 261-272.

Wu, Z., 2018. Drop "impact" on an airfoil surface. Advances in Colloid and Interface Science 256, 23-47.

Xu, L., Zhang, W.W., Nagel, S.R., 2005. Drop splashing on a dry smooth surface. Physical Review Letters 94, 184505.

Yarin, A.L., 2006. Drop impact dynamics: splashing, spreading, receding, bouncing…. Annual Review of Fluid Mechanics 38, 159-192.

Yeganehdoust, F., Attarzadeh, R., Karimfazli, I., Dolatabadi, A., 2020. A numerical analysis of air entrapment during droplet impact on an immiscible liquid film. International Journal of Multiphase Flow 124, 103175.

Youngs, D.L., 1984. an interface tracking method for a 3d eulerian hydrodynamics code. Technical Report 44/92/35.